ADVANCED BIOLOGY
www.advanced-bio.com

Flagellar Propulsion of Sperm Cells Against a Time-Periodic Interaction Force

Zihan Wang, Anke Klingner, Veronika Magdanz, Merijn W. Hoppenreijs, Sarthak Misra, and Islam S. M. Khalil**

Sperm cells undergo complex interactions with external environments, such as a solid-boundary, fluid flow, as well as other cells before arriving at the fertilization site. The interaction with the oviductal epithelium, as a site of sperm storage, is one type of cell-to-cell interaction that serves as a selection mechanism. Abnormal sperm cells with poor swimming performance, the major cause of male infertility, are filtered out by this selection mechanism. In this study, collinear bundles, consisting of two sperm cells, generate propulsive thrusts along opposite directions and allow to observe the influence of cell-to-cell interaction on flagellar wave-patterns. The developed elasto-hydrodynamic model demonstrates that steric and adhesive forces lead to highly symmetrical wave-pattern and reduce the bending amplitude of the propagating wave. It is measured that the free cells exhibit a mean flagellar curvature of 6.4 ± 3.5 rad mm^{-1} and a bending amplitude of 13.8 ± 2.8 rad mm^{-1}. After forming the collinear bundle, the mean flagellar curvature and bending amplitude are decreased to 1.8 ± 1.1 and 9.6 ± 1.4 rad mm^{-1}, respectively. This study presents consistent theoretical and experimental results important for understanding the adaptive behavior of sperm cells to the external time-periodic force encountered during sperm–egg interaction.

1. Introduction

In nature, microorganisms are capable of being propelled by the helical or wave-like motion of one or more flagella, as it is found in many bacteria,[1] algae,[2] and sperm cells.[3] They exhibit distinct wave-patterns that respond to external stimuli, including chemicals,[4–7] hydrodynamic drag,[8] temperature,[9] or mechanical forces.[10–12] For instance, the flagella of *Salmonella typhimurium* are normal left-hand helices at the solution with a neutral pH. In weakly acidic and alkaline conditions, the flagella are changed to coiled helices with a reduced pitch. The lower or higher pH environments transform the coiled helices into curly right-hand helices. Bacteria with the flagella of normal helices can perform smooth swimming, yet the coiled and curly helices are used in the tumbling motion to seek a new direction in response to chemotaxis.[13,14] The drastically polymorphic transformation of microorganisms can either optimize their motility or improve their survivability. For example, the parasite *Trypanosoma brucei* utilizes a long slender flagellum to propel itself in bodily fluids and penetrate the blood vessel to invade extravascular tissue. After entering the bloodstream with heterogeneous biochemical composition, the long slender flagellum of the parasite is transformed into a shorter stumpy one to ensure its survival.[15]

As an important role in fertilization, sperm cells swim in male and female reproductive tracts under the influence of physical or chemical stimuli. They are able to respond to stimuli (such as chemoattractant molecules, fluid flow, temperature, and surface) and use these signals to navigate to the ovum and achieve fertilization. For example, chemical gradients in the sex hormone progesterone direct sperm cells toward the ovum.[16] Chemotaxis provides a short-distance guidance mechanism for spermatozoa. The changes in calcium ion concentration induced by the presence of the chemoattractant can modulate the wave-patterns of sperm cells, thus resulting in different swimming paths and redirecting sperm

Z. Wang, S. Misra
Surgical Robotics Laboratory
Department of Biomedical Engineering
University of Groningen and University Medical Center Groningen
9713 GZ Groningen, The Netherlands

A. Klingner
Department of Physics
The German University in Cairo
New Cairo 13411, Egypt

The ORCID identification number(s) for the author(s) of this article can be found under https://doi.org/10.1002/adbi.202200210.

DOI: 10.1002/adbi.202200210

V. Magdanz
Smart Nano-Bio-Devices Group
Institute for Bioengineering of Catalonia
08028 Barcelona, Spain

V. Magdanz
University of Waterloo
Systems Design Engineering
200 University Avenue West Waterloo
Ontario N2L3G1, Canada
E-mail: veronika.magdanz@uwaterloo.ca

M. W. Hoppenreijs, S. Misra, I. S. M. Khalil
Surgical Robotics Laboratory
Department of Biomechanical Engineering
University of Twente
7522 NB Enschede, The Netherlands
E-mail: i.s.m.khalil@utwente.nl

cells to the source of the attractant (i.e., the ovum). Additionally, rheotaxis has been found to serve as a long-distance guidance mechanism, as motile sperm cells are able to swim against the fluid flow present in the female reproductive tract.[17] When the temperature increases, the wave amplitude near the proximal end decreases. Consequently, sperm cells would swim with an enhanced velocity and linearity due to the decrease in the side-to-side displacement of the proximal end.[18] A temperature gradient has been found in several mammalian female reproductive tracts, and sperm cells swim to the warmer region at the oviduct,[19] assuming that thermotaxis is an additional mechanism for guidance. Swimming along surfaces is known as a physical guidance mechanism of sperm cells.[20] It has been observed that sperm cells rotate to become nearly tangential to the surface.

To explicitly elucidate the locomotion behavior of microorganisms with a single flagellum or multiple flagella, elasto-hydrodynamic models are developed to study the hydrodynamic interaction between the elastic flagella and surrounding fluid. By combining the hydrodynamic computation and the high-speed tracking experiments, Friedrich et al. have concluded that cell-body rocking plays a major role in the flagellar synchronization of green algae *Chlamydomonas reinhardtii* instead of the direct hydrodynamic interaction.[21] Hilfinger et al.[22] have developed a nonlinear wave equation to describe wave-patterns of sperm cells. They have presented the numerical results of the nonlinear wave equation at different boundary conditions and found the reconstructed wave-pattern through the equation are approximated by those observed experimentally. Later, Walker et al.[23] have extended the elasto-hydrodynamic model of sperm cells to the 3D space, such that the model can explain complex 3D motion of sperm cells. In the female reproductive tracts, sperm cells inevitably interact with other cells before achieving fertilization. However, the effect of cell-to-cell interaction on wave-patterns of sperm cells has not been investigated, and the relevant elasto-hydrodynamic model has not been developed.

Infertility is a universal health issue affecting 48 million couples and 186 million individuals.[24] Half of the infertile couples have low sperm count, abnormal sperm cells with poor motility, or blockages along the reproductive tract. In this work, we investigate the wave-pattern of sperm cells under a time-periodic interaction force. This time-periodic interaction is observed in a bundle of bovine sperm cells assembled in the opposite directions (**Figure 1**). An elasto-hydrodynamic model is developed to interpret the interactions between the elastic forces of sperm flagella, the interaction forces of two cells, and the hydrodynamic drag forces of the surrounding fluids. We use Fourier analysis of the measured wave-pattern in two types of fluids with low and high viscosity, and measure the wave variables of the free cells that are not affected by time-periodic interaction forces and compare that to the case where the cells form the collinear bundles. Our model can explain the variation of wave-pattern of sperm cells after forming a collinear bundle. Moreover, we provide new tools to assess the motility of sperm cells by analyzing the flagellar motion and advance the understanding of cell-to-cell interaction in reproductive health.

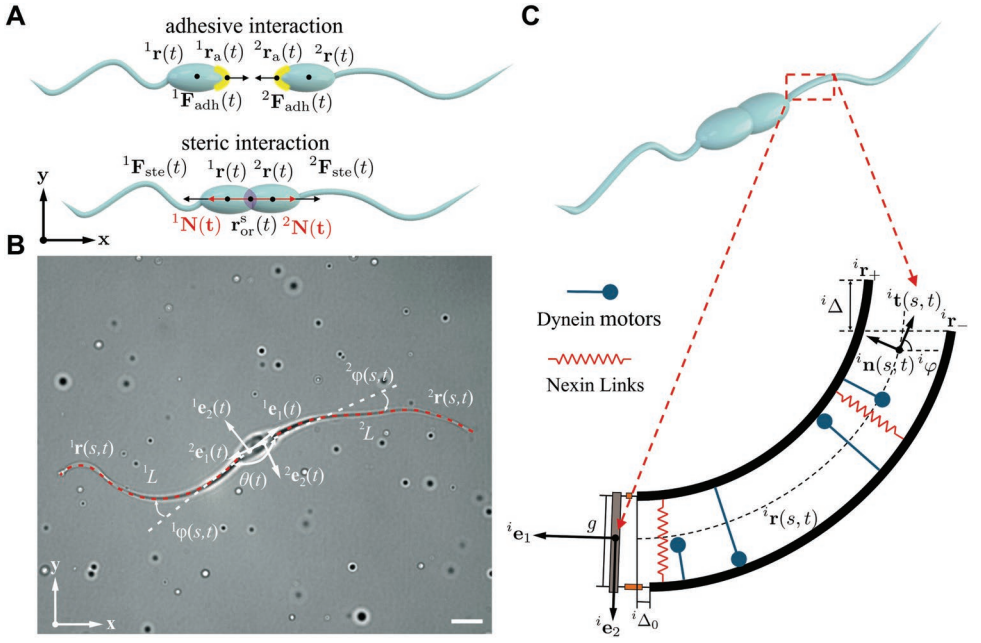

Figure 1. The modeling of a collinear bundle with two flagella in opposite directions. A) Adhesive and steric interaction of two cells. Due to the existence of the adhesive regions (the yellow-labeled part), the adhesive forces ${}^1\mathbf{F}_{adh}(t)$ and ${}^2\mathbf{F}_{adh}(t)$ are generated on the position ${}^1\mathbf{r}_a(t)$ and ${}^2\mathbf{r}_a(t)$, respectively. The steric forces ${}^1\mathbf{F}_{ste}(t)$ and ${}^2\mathbf{F}_{ste}(t)$ are applied to the centroid $\mathbf{r}^s_{or}(t)$ of the overlapped region (the purple part) with the direction vectors ${}^1\mathbf{N}(t)$ and ${}^2\mathbf{N}(t)$, respectively. The position vectors ${}^1\mathbf{r}(t)$ and ${}^2\mathbf{r}(t)$ denote the centers of the sperm heads of two cells, respectively, in the laboratory frame of reference $(\mathbf{x}, \mathbf{y})$. B) Two bovine sperm cells adhere to each other into a collinear bundle in which the transverse waves propagate in opposite directions. The wave propagation of two cells is characterized by the tangent angles ${}^1\varphi(s, t)$ and ${}^2\varphi(s, t)$, respectively, along the arclength s at time instant t. Two tangent angles ${}^1\varphi(s, t)$ and ${}^2\varphi(s, t)$ are described at the position ${}^1\mathbf{r}(s,t)$ and ${}^2\mathbf{r}(s,t)$ with respect to the body frames of reference $({}^1\mathbf{e}_1, {}^1\mathbf{e}_2)$ and $({}^2\mathbf{e}_1, {}^2\mathbf{e}_2)$, respectively. The angle $\theta(t)$ denotes the relative orientation of two sperm heads. The scale bar is 10 µm. C) Schematic representation of 2D projection of flagellar axoneme. Two polar filaments ${}^i\mathbf{e}_+$ and ${}^i\mathbf{r}_-$ with the distance of g are connected by nexin links. The length mismatch of two filaments at the proximal end is ${}^i\Delta_0$ and the sliding displacement at the distal end is ${}^i\Delta(s, t)$. The unit vectors ${}^i\mathbf{t}(s, t)$ and ${}^i\mathbf{n}(s, t)$ are the tangent and normal vector at the position of the segment on the flagellum, respectively.

2. Actively Propagated Waves along Two Collinear Flagella

2.1. Cell-to-Cell Interactions

Sperm cells produce propagating waves toward the distal end of the flagellum to push the cell forward. During cell-to-cell interaction, two cells can form a collinear bundle with two flagella in opposite orientations by means of the head-to-head attachment. Steric and adhesive interactions are two essential effects in this attachment manner.[25] One cell is attracted to the other by adhesive molecules located at the adhesive region, as shown in Figure 1A. Adhesive regions have been observed on the acrosome, the tip region of bovine sperm heads.[26] The position vectors ${}^{i}\mathbf{r}_{a}(t)$ and ${}^{j}\mathbf{r}_{a}(t)$ are the closest pair of vertices within the adhesive region of two cells. The adhesive force ${}^{i}\mathbf{F}_{adh}(t)$ is applied to the sperm head of the ith cell, which points from ${}^{i}\mathbf{r}_{a}(t)$ to ${}^{j}\mathbf{r}_{a}(t)$, while the adhesive torque ${}^{i}\mathbf{M}_{adh}(t)$ is generated on the center ${}^{i}\mathbf{r}(t)$ of ith sperm head. The adhesive force and torque are given by the following expressions:

$$ {}^{i}\mathbf{F}_{adh}(t)=\kappa_{a}({}^{j}\mathbf{r}_{a}(t)-{}^{i}\mathbf{r}_{a}(t)),\ {}^{i}\mathbf{M}_{adh}(t)=({}^{i}\mathbf{r}_{a}(t)-{}^{i}\mathbf{r}(t))\times{}^{i}\mathbf{F}_{adh}(t)(i=1,2) \quad (1) $$

where κ_{a} is the adhesive elastic constant of the sperm head. The adhesive force is produced only if $|{}^{i}\mathbf{r}_{a}(t)-{}^{j}\mathbf{r}_{a}(t)|<l_{a}$, and l_{a} is the characteristic distance where the adhesive connection of two cells breaks down. The adhesive interaction contributes to the approaching of two cells. Regarding the steric interaction of two cells, the steric force ${}^{i}\mathbf{F}_{ste}(t)$ is imposed on the vector position $\mathbf{r}_{or}^{c}(t)$, the centroid of the overlapped region. The unit vector ${}^{i}\mathbf{N}$ normal to the overlapped region of the two sperm heads denotes the direction of the steric force ${}^{i}\mathbf{F}_{ste}(t)$ (see Figure 1A). The steric force ${}^{i}\mathbf{F}_{ste}(t)$ imposed on the ith cell results from the steric interaction with the jth cell, while the steric torque ${}^{i}\mathbf{M}_{ste}(t)$ acts on the center ${}^{i}\mathbf{r}(t)$ of sperm head. The force and torque arising from the steric interaction can be as follows:[25]

$$ {}^{i}\mathbf{F}_{ste}(t)=0.5\kappa_{c}({}^{i}v(t)+{}^{j}v(t))\Delta t\,{}^{i}\mathbf{N}(t),\ {}^{i}\mathbf{M}_{ste}(t)=(\mathbf{r}_{or}^{s}(t)-{}^{i}\mathbf{r}(t))\times{}^{i}\mathbf{F}_{ste}(t) \quad (2) $$

where κ_{c} is the steric elastic constant of the sperm head, Δt is the time step, and ${}^{i}v(t)$ and ${}^{j}v(t)$ are the average path velocity of ith and jth cell with respect to the laboratory frame of reference (**x**,**y**) in Figure 1B, respectively. Affected by the steric interaction, two cells behave mutual exclusion and separate apart. The forces and torques generated during the interaction act on the sperm cell and affect the wave-pattern as external stimuli. To characterize wave-patterns of sperm cells during cell-to-cell interaction, the elasto-hydrodynamics, which deal with the interaction between actively elastic flagellum, the hydrodynamic drag, and the other cell, is studied below.

2.2. The Elasto-Hydrodynamic Flagellum

Although it is unknown whether sperm bundles can fertilize the ovum, the bundle formation is likely to enhance the swimming speed of the cells.[27,28] Multiple sperm cells can form a collinear bundle without the need for any external stimuli. The unique configuration of collinear bundles allows us to understand the swimming behavior when the head is not free. In our experiments, the collinear bundle consists of two bovine sperm cells with opposite directions. The body frames of reference $({}^{1}\mathbf{e}_{1},{}^{1}\mathbf{e}_{2})$ and $({}^{2}\mathbf{e}_{1},{}^{2}\mathbf{e}_{2})$ of the two cells are located at the centers ${}^{1}\mathbf{r}(t)$ and ${}^{2}\mathbf{r}(t)$, respectively, of their heads such that the orthonormal vectors ${}^{1}\mathbf{e}_{1}$ and ${}^{2}\mathbf{e}_{1}$ are oriented along the major axis of the sperm head of the first and second cell, respectively. Two ellipsoidal sperm heads with major diameter $2a$ and minor diameter $2b$ are connected to the flagella of length ${}^{1}L$ and ${}^{2}L$ at $-a{}^{1}\mathbf{e}_{1}$ and $-a{}^{2}\mathbf{e}_{1}$, respectively, as shown in Figure 1B. The relative orientation of two cells is characterized by $\theta(t)$, which is the angle between the orthonormal vectors ${}^{1}\mathbf{e}_{1}$ and ${}^{2}\mathbf{e}_{1}$. The flagellar axoneme can be regarded as two filaments including distributed contractile elements to induce transverse propagating waves and generate flagellar propulsion. Figure 1C shows the planar projection of the flagellar axoneme. Two polar filaments ${}^{i}\mathbf{r}_{+}$ and ${}^{i}\mathbf{r}_{-}$ of the flagellar axoneme are connected by elastic nexin links with the constant distance of g.[29] Once the sliding displacement ${}^{i}\Delta(s,t)$ exists between two polar filaments, the bending force is generated and causes the flagellum bending. The bending force density, ${}^{i}f_{ben}(s,t)=k{}^{i}\Delta(s,t)$, is proportional to the sliding displacement with elastic sliding resistance k. Moreover, the sliding displacement can be determined through the tangent angle ${}^{i}\varphi$. The expression of sliding displacement is given by[30]

$$ {}^{i}\Delta(s,t)=\int_{0}^{s}(|\partial_{s}^{i}\mathbf{r}_{-}|-|\partial_{s}^{i}\mathbf{r}_{+}|)\mathrm{d}s'={}^{i}\Delta_{0}(t)+g({}^{i}\varphi(s,t)-{}^{i}\varphi_{0}(t)) \quad (3) $$

where ${}^{i}\Delta_{0}$ and ${}^{i}\varphi_{0}$ are the length mismatch of two polar filaments and tangent angle of the centerline at the proximal end, respectively. The internal force, which is composed of the elastic force and the bending force, along the flagellum can be expressed as follows:

$$ {}^{i}\mathbf{F}_{int}=(-{}^{i}E{}^{i}\varphi_{ss}+{}^{i}f_{ben}(s,t)g)\,{}^{i}\mathbf{n}(s,t) \quad (4) $$

where ${}^{i}E$ is the bending stiffness of the ith flagellum, the subscript s denotes arclength derivative, and ${}^{i}\mathbf{n}(s,t)$ is the unit normal vector along the arclength s of the ith flagellum at the time instant t.

Sperm flagellum oscillates in a time-periodic manner such that the elastic force and the bending force are balanced by the viscous drag force determined by the resistive-force theory[31] (see Experimental section). Note that the elastic force tends to straighten the flagellum, the bending force is the cause of the propagating waves, and the viscous drag force propels sperm cells forward. The average path velocity, v, of the collinear bundle is relatively small because the two cells are swimming along opposite directions. The force dipole field strength generated by the ith cell scales as $|{}^{i}p|\sim\eta v{}^{i}L^{2}$,[32] where η is the viscosity of the fluid and is lower than that of a free sperm cell owing to the low average path velocity of the collinear bundle (Figure 1B). In addition, since the collinear bundle consists of two sperm cells along the opposite directions, their flagella are far from each other, and the hydrodynamic interaction between the two flagella is negligible compared to the direct head-to-head interaction. Therefore, the resistive force theory is applicable to calculate the resistive drag for a given flagellum geometry.

The flagellum elasto-hydrodynamics are governed by the balance of elastic force, bending force, and viscous drag force on every segment, and we have

$$-{}^{i}E\,{}^{i}\varphi_{ssss} + g^{2}\,{}^{i}k\,{}^{i}\varphi_{ss} = {}^{i}\xi_{\perp}\,{}^{i}\varphi_{t} \tag{5}$$

where ${}^{i}\xi_{\perp}$ is the normal drag coefficient of the ith flagellum. The governing equation can be numerically solved after specifying four boundary conditions. Wave-pattern can be reconstructed based on the solved tangent angle ${}^{i}\varphi(s, t)$. The distal end of the flagellum is free from force and torque owing to the lack of motor elements. Thus, we have the following boundary equations,

$$-{}^{i}E\,{}^{i}\varphi_{ss}({}^{i}L,t) + g\,{}^{i}f_{ben}({}^{i}L,t) = 0 \tag{6}$$

$$-{}^{i}E\,{}^{i}\varphi_{s}({}^{i}L,t) = 0 \tag{7}$$

The proximal end of the flagellum experiences drag force of the sperm head, steric force and adhesive force when interacting with the other cell. Additionally, we assume that the proximal end of sperm cell is fixed over the course of movement. Therefore, the boundary equations on the proximal end are given by

$$-{}^{i}E\,{}^{i}\varphi_{ss}(0,t) + g\,{}^{i}f_{ben}(0,t) = -({}^{i}\mathbf{F}(t) + {}^{i}\mathbf{F}_{ste}(t) + {}^{i}\mathbf{F}_{adh}(t))\cdot {}^{i}\mathbf{n}(0,t) \tag{8}$$

$$-{}^{i}E\,{}^{i}\varphi_{sss}(0,t) + g^{2}\,{}^{i}k\,{}^{i}\varphi_{s}(0,t) = 0 \tag{9}$$

where ${}^{i}\mathbf{F}$ is the drag force acting on the flagellum of the ith cell by the sperm head. For a sperm cell, the drag force ${}^{i}\mathbf{F}$ can be expressed as follows:

$${}^{i}\mathbf{F}(t) = ({}^{i}F_{amp}\cos(\omega t + {}^{i}\theta_{pha}) + {}^{i}F_{off})\,{}^{i}\mathbf{n}(0,t) \tag{10}$$

where ${}^{i}F_{amp}$ and ${}^{i}F_{off}$ are the force amplitude and force offset of the drag force ${}^{i}\mathbf{F}(t)$, respectively, and ω is the angular frequency of the flagellar beat. The angle ${}^{i}\theta_{pha}$ is the initial phase of sinusoidal variation of the drag force. In the case of free cells, we have two equations ${}^{i}\mathbf{F}_{ste}(t) = \mathbf{0}$ and ${}^{i}\mathbf{F}_{adh}(t) = \mathbf{0}$. With these boundary equations, the wave-pattern of the sperm bundle can be reconstructed in the laboratory frame of reference $(\mathbf{x}, \mathbf{y})$ by solving the governing equation. The kinematics of a sperm bundle are introduced in detail at the next section.

2.3. Kinematics of Sperm Bundles

The position vectors of two flagellar centerlines with respect to the body frames of reference are determined by[33]

$${}^{i}\mathbf{r}(s,t) = {}^{i}\mathbf{r}(t) - a\,{}^{i}\mathbf{e}_{1}(t) - \int_{0}^{s}\cos{}^{i}\varphi(\ell,t)\,{}^{i}\mathbf{e}_{1}(t) + \sin{}^{i}\varphi(\ell,t)\,{}^{i}\mathbf{e}_{2}(t)\mathrm{d}\ell \tag{11}$$

Equation (11) gives the flagellar kinematics of a sperm bundle. The total force and moment of the bundle should be studied to further investigate its swimming characteristic. Each cell in a sperm bundle experiences the propulsive thrust ${}^{i}\mathbf{F}_{pro}(t)$ along the sperm flagellum, the viscous drag force ${}^{i}\mathbf{F}_{hea}(t)$ on the sperm head, and the interaction force ${}^{i}\mathbf{F}_{ste}(t)$ and ${}^{i}\mathbf{F}_{adh}(t)$ exerted by the other cell. Thus, the force balance equation of each cell can be described as follows:

$${}^{i}\mathbf{F}_{tot}(t) = {}^{i}\mathbf{F}_{pro}(t) + {}^{i}\mathbf{F}_{hea}(t) + {}^{i}\mathbf{F}_{ste}(t) + {}^{i}\mathbf{F}_{adh}(t) = 0 \tag{12}$$

The total propulsive thrust ${}^{i}\mathbf{F}_{pro}(t)$ can be calculated through the integral of the propulsive force density ${}^{i}\mathbf{f}(s,t)$ along the flagellum length. The propulsive force density ${}^{i}\mathbf{f}(s,t)$ is derived from the resistive-force theory. In addition, the viscous drag force ${}^{i}\mathbf{F}_{hea}(t)$ on the sperm head of the ith cell is given by

$${}^{i}\mathbf{F}_{hea}(t) = 6\pi a\eta C_{1}^{i}\mathbf{v}_{1}(t) + 6\pi a\eta C_{2}^{i}\mathbf{v}_{2}(t) \tag{13}$$

where ${}^{i}\mathbf{v}_{1}(t)$ and ${}^{i}\mathbf{v}_{2}(t)$ are the translational velocity and the transverse velocity of ith cell along ${}^{i}\mathbf{e}_{1}$ and ${}^{i}\mathbf{e}_{2}$, respectively. The coefficients C_1 and C_2 are the geometric parameters of the ellipsoid heads of the sperm cells. To further determine the angular speeds of two sperm cells, the moment balance equation for each cell is constructed. The moment balance equation on the ith cell can be expressed as follows:

$${}^{i}\mathbf{M}_{tot}(t) = {}^{i}\mathbf{M}_{hea}(t) + {}^{i}\mathbf{M}_{ste}(t) + {}^{i}\mathbf{M}_{adh}(t) + \int_{0}^{{}^{i}L^{i}}\mathbf{r}(s,t)\times{}^{i}\mathbf{f}(s,t)\mathrm{d}s = 0 \tag{14}$$

where ${}^{i}\mathbf{M}_{hea}(t)$ is the viscous drag torque on the sperm head of the ith cell. According to the low Reynold number (Re) hydrodynamics, the viscous drag torque ${}^{i}\mathbf{M}_{hea}(t)$ is proportional to the angular speed ${}^{i}\omega_{hea}(\mathbf{t})$ of the sperm cell as ${}^{i}\mathbf{M}_{hea}(t) = 8\pi\eta ab^{2}C_{3}\,{}^{i}\omega_{hea}(t)$, where the coefficient C_3 represents the geometric parameter of the sperm head. Through Equations (12)–(14), the translational, the transverse, and the angular speed of the two cells can be calculated. Then, the body frames of reference of two cells at every time instant can be known after determining the positions and orientations of two sperm heads. The modeling of the interaction of two cells is completely established.

2.4. Numerical Results

2.4.1. The Formation of Collinear Bundles

In the presence of steric and adhesive interaction, two cells can form a sperm bundle through the head-to-head attachment. **Figure 2**A shows the relative orientation of the two cells with initial orientation θ_0 ranging from 30° to 150° over the formation of the sperm bundle. Regardless of the initial orientation θ_0, the configuration of the sperm bundle depends on the resultant interaction torque, ${}^{i}\mathbf{M}_{ite} = {}^{i}\mathbf{M}_{adh} - {}^{i}\mathbf{M}_{ste}$. We give a detailed explanation of the formation of a collinear bundle and an aligned bundle when θ_0 is 90°. Initially, the first cell is oriented horizontally, while the second cell swims vertically. When the adhesive torque ${}^{i}\mathbf{M}_{adh}$ is overwhelmed by the torque ${}^{i}\mathbf{M}_{ste}$ resulting from the steric force, the collinear bundle is formed. The head-to-head interaction of the two cells is illustrated in Figure 2B. The first cell (the red) rotates clockwise under the effect of the negative torque ${}^{1}\mathbf{M}_{ite}$. Since the steric and adhesive torques acting on the second cell (the blue) are opposite to those on the first cell, the second cell rotates counter-clockwise

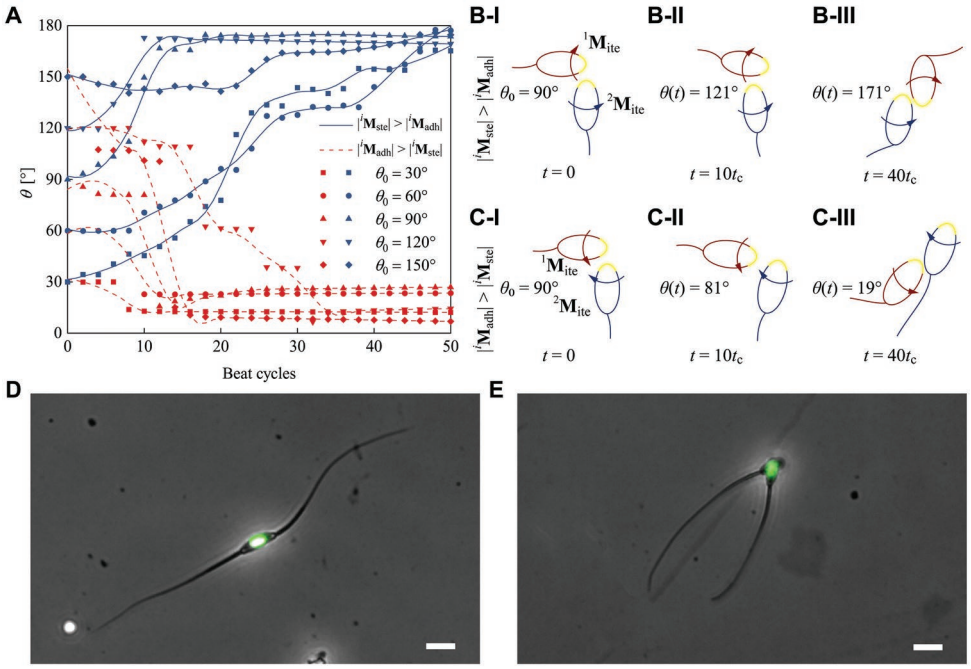

Figure 2. Two types of sperm bundles. A) The numerical results of the relative orientation $\theta(t)$ of two sperm heads with initial orientation θ_0. B) The relative orientation of two sperm heads in time sequences when the steric torque $|^i\mathbf{M}_{ste}|$ is greater than the adhesive torque $|^i\mathbf{M}_{adh}|$. The resultant interaction torques $^1\mathbf{M}_{ite}$ and $^2\mathbf{M}_{ite}$, $^i\mathbf{M}_{ite} = {}^i\mathbf{M}_{adh} - {}^i\mathbf{M}_{ste}$, with opposite directions are applied to the sperm heads of the first and second cell, respectively. We assume that counterclockwise rotation is the positive rotation direction. Therefore, the first cell rotates clockwise under the effect of the negative resultant torque, and the second cell rotates counterclockwise. The relative orientation $\theta(t)$ increases in three beat cycles, and the time of one beat cycle is t_c. C) The relative orientation of two sperm heads in time sequences when $|^i\mathbf{M}_{adh}| > |^i\mathbf{M}_{ste}|$. In this case, the first cell rotates counterclockwise, and the second cell rotates clockwise. The relative orientation $\theta(t)$ decreases in three beat cycles. The fluorescent images of D) the collinear bundle and E) the aligned bundle. The scale bar is 10 μm.

after experiencing the positive torque $^2\mathbf{M}_{ite}$. The relative orientation between two cells increases progressively in time sequences and finally oscillates around 180°. Conversely, two cells will form the aligned bundle if $|^i\mathbf{M}_{adh}| > |^i\mathbf{M}_{ste}|$. Because the torque arising from the adhesive force is predominant, the first cell rotates counter-clockwise, and the second cell displays the contrary rotation, as depicted in Figure 2C. The relative orientation of two cells decreases from 90° to around 19°, and finally oscillates around 25°. Two representative configuration of sperm bundle can be seen in Figure 2D,E. We demonstrate that the configuration of sperm bundle is decided by the resultant torque due to the steric and adhesive interaction, irrespective of the initial orientations of two cells.

2.4.2. The Influence of a Time-Periodic Force

In nature, two cells can form a bundle through the head-to-head, tail-to-tail, and head-to-tail attachment. However, the vast majority of motile sperm cells form bundles by attachments between the heads. Moreover, under the head-to-head attachment, one cell experiences the time-periodic force generated by the other cell with the time-periodic flagellar deformation. Therefore, the collinear bundle provides a unique opportunity to investigate the response of sperm cells to an external time-periodic force exerted on the sperm head. We show the numerical results when two cells form a collinear bundle. The flagellar deformation at every beat cycle is obtained upon solving the governing equation, while the kinematics of two cells are determined through Equations (12)–(14). Using the developed model, we simulate the interaction of two cells for continuous beat cycles, and study the variation of wave-pattern of sperm cells after forming the collinear bundle. In the simulation, two cells are initially placed with the opposite orientations. The entire movement can be divided into two phases. The first phase shows the free swimming of the two cells, and the wave-patterns of the two cells are presented in **Figure 3**A. The second phase is when the two cells form the collinear bundle, that is to say, the adhesive forces and steric forces are applied additionally to the sperm cells. Figure 3A also shows the wave-patterns of the two cells after forming the collinear bundle. When the interaction occurs, the adhesive force is first produced and acts to pull two cells closer. Subsequently, the steric force arises owing to the overlap of two sperm heads. Since the steric force is stronger than the adhesive force, two cells separate until the adhesive force is dominant again. Two cells go through the above interaction periodically.

In terms of the governing equation, the force, $^i\mathbf{F}_{prx}(t) = {}^i\mathbf{F}(t) + {}^i\mathbf{F}_{adh}(t) + {}^i\mathbf{F}_{ste}(t)$, on the proximal end modulates the flagellar deformation of the sperm cell. Figure 3B shows the variation of force $^1\mathbf{F}_{prx}$ exerted on the first cell. When two cells freely swim, the force $^1\mathbf{F}_{prx}$ only comprises the drag force $^1\mathbf{F}$, which shows the sinusoidal variation with time. After that, the two cells start to interact, and adhesive force and steric force are

added to the drag force. Therefore, wave-pattern of sperm cells changes after forming the collinear bundle. The force ${}^{1}\mathbf{F}_{prx}$ oscillates with the angular frequency ${}^{1}\omega$ of the flagellar beat, which is reflected by the power spectrum in Figure 3B. Also, we display the variation of the interaction force, ${}^{i}\mathbf{F}_{ite}(t) = {}^{i}\mathbf{F}_{adh}(t) + {}^{i}\mathbf{F}_{ste}(t)$, on the first cell with respect to time in Figure 3B. The curve implies that the first cell experiences the time-periodic interaction force after forming the collinear bundle. Therefore, the collinear bundle can be a qualified objective to study the effect of a time-periodic force on the wave-pattern.

Next, the Fourier analysis (see Experimental section) is used to analyze the wave-pattern obtained from the numerical results. Figure 3C displays variation of wave variables of two sperm cells over 100 beat cycles. The wave-patterns are time-periodic when two cells freely swim, whereas the wave variables become unsteady after forming the collinear bundle. It can be attributed to the varying interaction force on the two sperm heads. When freely swimming, the mean flagellar curvature ${}^{1}K_0$, the bending amplitude ${}^{1}A_0$, and the wavelength ${}^{1}\lambda$ are 0.88 rad mm^{-1}, 7.55 rad mm^{-1}, and 52.29 μm, respectively, and ${}^{2}K_0$, ${}^{2}A_0$, and ${}^{2}\lambda$ are 1.00 rad mm^{-1}, 7.07 rad mm^{-1}, and 55.20 μm, respectively. The discrepancy in the wave variables of the two cells is caused by the different bending stiffness, ${}^{1}E = 1.8 \times 10^{-21}$ N m^2 and ${}^{2}E = 2.5 \times 10^{-21}$ N m^2. Subsequently, the steric and adhesive force are imposed on the sperm cells. The wave variables ${}^{1}K_0$ and ${}^{1}A_0$ are decreased to 0.48 ± 0.15 rad mm^{-1} and 7.12 ± 0.12 rad mm^{-1}, respectively, and ${}^{1}\lambda$ is kept at 52.23 ± 0.04 μm. The interaction causes an impact on the wave-patterns of the second cell as well. During the interaction, the wave variables ${}^{2}K_0$, ${}^{2}A_0$, and ${}^{2}\lambda$ are 0.55 ± 0.17 rad mm^{-1}, 6.67 ± 0.14 rad mm^{-1}, and 55.15 ± 0.05 μm, respectively. Therefore, the mean flagellar curvature K_0 and the bending amplitude A_0 of two cells are reduced, but there is no obvious difference on the wavelength λ after forming the collinear bundle.

The average value $\langle \mathbf{F}_{prx} \rangle$ and the root mean square RMS($\mathbf{F}_{prx}$) of the force on the proximal end can explain the variation of K_0 and A_0 after forming the collinear bundle, respectively. The average force $\langle \mathbf{F}_{prx} \rangle$ denotes the time-symmetry of the force. A time-symmetrical force on the proximal end leads to the symmetrical wave-patterns, since the propagating wave is directly modulated by the force on the proximal end. Therefore, the closer $\langle \mathbf{F}_{prx} \rangle$ is to 0, the smaller K_0 is. The average force $\langle {}^{1}\mathbf{F}_{prx} \rangle$ applied to the proximal end of first cell is 1.0×10^{-12} N during the free swimming. It decreases to 5.2×10^{-13} N after forming the collinear bundle. For the second cell, the average

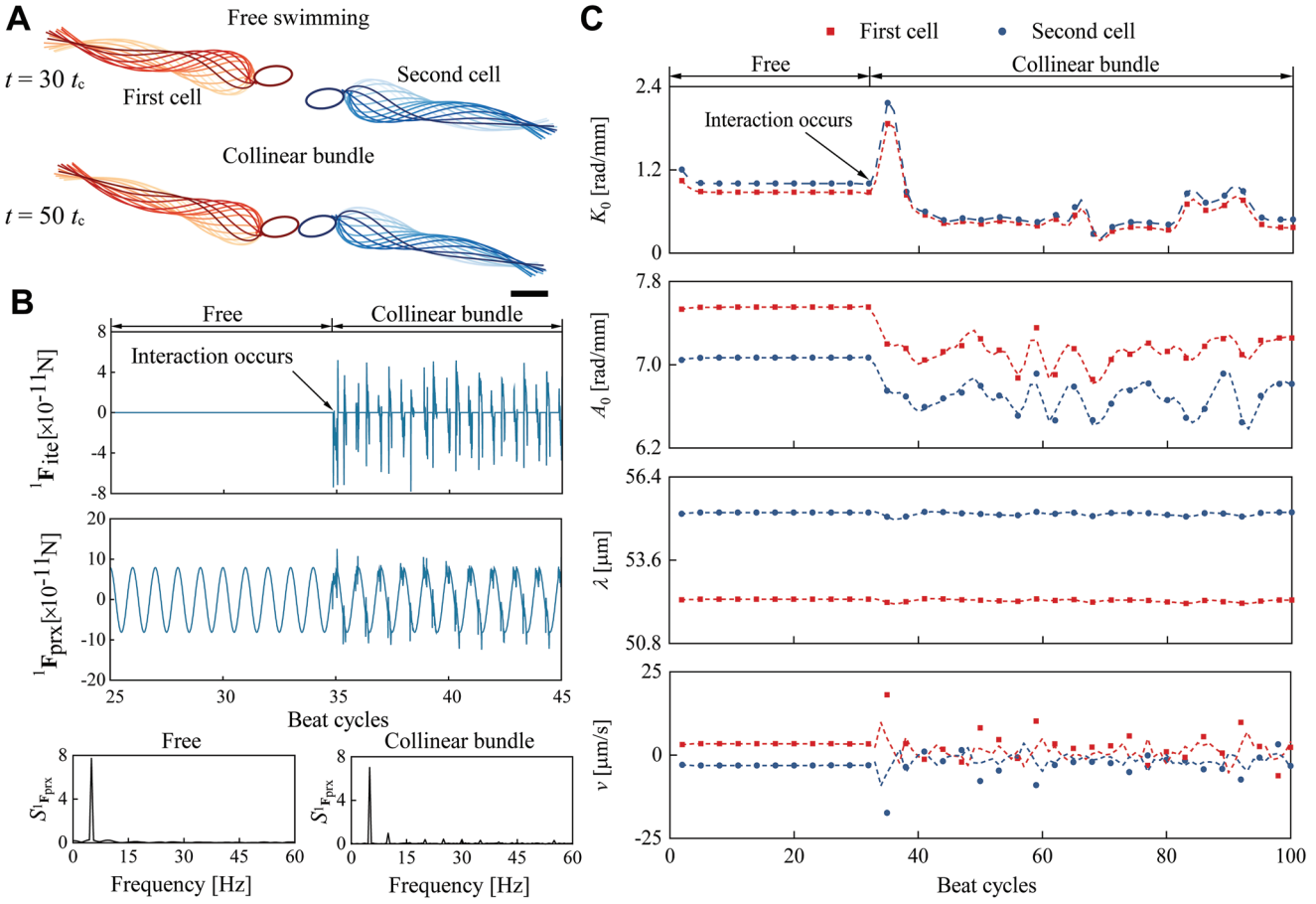

Figure 3. The numerical results by modeling the interaction of two sperm cells. A) The simulated wave-patterns of two cells when freely swimming and after forming the collinear bundle (darker curves for later times). The scale bar is 10 μm. B) The interaction force ${}^{1}\mathbf{F}_{ite}$ on the sperm head of the first cell and the force ${}^{1}\mathbf{F}_{prx}$ on the proximal end of the first cell. Power spectrum of ${}^{1}\mathbf{F}_{prx}$ during the free swimming and after forming the collinear bundle. C) The mean flagellar curvature K_0, the bending amplitude A_0, and the wavelength λ of the simulated wave-pattern are extracted over one hundred beat cycles. The average path velocities v of two cells decrease during the interaction.

force $\langle {}^2\mathbf{F}_{prx}\rangle$ is decreased from 1.0×10^{-12} to 5.4×10^{-13} N. It agrees well with the decrease of the mean flagellar curvatures ${}^1K_0$ and ${}^2K_0$. The decrease of the average force can be attributed to the addition of the interaction force after forming the collinear bundle. On the other hand, the root mean square of force $\mathrm{RMS}(\mathbf{F}_{prx})$ denotes the force amplitude, which affects the bending amplitude of the propagating wave. The values of $\mathrm{RMS}(\mathbf{F}_{prx})$ for both two cells decrease from approximately 5.7×10^{-11} to 5.5×10^{-11} N after forming the collinear bundle. The interaction force ${}^i\mathbf{F}_{ite}(t)$ against the drag force ${}^i\mathbf{F}(t)$ causes the attenuation of force amplitude, thereby resulting in the decrease of the bending amplitude A_0. Figure 3C also describes the swimming characteristic of two cells over one hundred beat cycles. Affected by steric and adhesive force, the average path velocities of sperm cells strongly weaken after forming the collinear bundle.

Besides, our developed model can predict the effect of other parameters on wave-pattern of sperm cells after forming the collinear bundle. The phase shift, $\Delta\theta_{pha} = {}^2\theta_{pha} - {}^1\theta_{pha}$, between the propagating waves of two cells and the elastic sliding resistance k are changed in our model. In the context below, the variation extent of the wave variables is expressed through the percentage. The phase shift $\Delta\theta_{pha}$ ranges from 0° to 180° by keeping ${}^1\theta_{pha} = 0°$ and setting ${}^2\theta_{pha}\ \varepsilon\ [0°180°]$. The flagellar deformation is determined by the force acting on the proximal end of the flagellum. We use Equation (10) to express the force on the proximal end of free sperm cells. By varying the initial phase ${}^i\theta_{pha}$ in Equation (10), the initial phase of the propagating wave is changed with that of the force. The propagating wave at the latest time (see the darkest curves of the second cell in **Figure 4**A) moves from left to right, when the initial phase ${}^2\theta_{pha}$ increases from 0° to 180°. Therefore, the change of the initial phase is indicated by the shift of the propagating wave. Figure 4A shows the wave-patterns of two cells with different phase shifts $\Delta\theta_{pha}$ during the free swimming and after forming the collinear bundle. The variations of K_0 (ΔK_0) with $\Delta\theta_{pha}$ are displayed in Figure 4B-I. The negative percentage indicates that K_0 of the cell decreases after forming the collinear bundle irrespective of $\Delta\theta_{pha}$. To validate the relationship between the average force $\langle\mathbf{F}_{prx}\rangle$ and K_0, the variations of the average force $\Delta\langle\mathbf{F}_{prx}\rangle$ are shown in Figure 4B-II. The flagellar deformation at every time instant is determined by the instantaneous force $\mathbf{F}_{prx}$ imposed on the proximal end. If the force is symmetrical with respect to time, the time-symmetrical wave-pattern is formed. Therefore, when the average force $\langle\mathbf{F}_{prx}\rangle$ decreases, the wave-pattern of the cell will be more symmetrical. The bending amplitude A_0 increases during the interaction if the phase shift $\Delta\theta_{pha}$ exceeds 90°, as shown in Figure 4B-III. This reflects that the interaction force boosts the bending of the propagating wave in this case. Basically, the sperm cell changes the phase of wave-patterns by adjusting the initial phase ${}^i\theta_{pha}$ of the drag force ${}^i\mathbf{F}$. When the initial phase ${}^i\theta_{pha}$ exceeds 90°, the direction of the interaction force becomes the same as that of the drag force ${}^i\mathbf{F}$. Thus, the bending of the flagellum of the cell is facilitated after interacting with the other cell. Figure 4B-IV shows the variations of the root mean square of the force $\Delta\mathrm{RMS}(\mathbf{F}_{prx})$ versus different phase shifts $\Delta\theta_{pha}$. When $\Delta\theta_{pha}$ is greater than 90°, $\Delta\mathrm{RMS}({}^2\mathbf{F}_{prx})$ is positive, which is in agreement with the increase of ${}^2A_0$ after forming the collinear bundle.

The flagellar axoneme of sperm cells varies across species. In mammalian sperm cells, the axoneme is surrounded by outer dense fibers, mitochondria, and plasma membrane at the midpiece. The principal piece is surrounded by outer dense fibers, fibrous sheath, and plasma membrane, and the distal end is only enveloped by plasma membrane.[3] In terms of non-mammalian sperm cells, such as sea urchins, tunicates, and teleosts the axonemes are simply enclosed by a plasma membrane.[34] The outer surrounding is likely to resist the sliding of two polar filaments, resulting in the varying elastic sliding resistance k among different species. Regarding the different elastic sliding resistance k, the wave-patterns of two cells are shown in **Figure 5**A during the free swimming and after forming the collinear bundle. Upon increasing the elastic sliding resistance, it is harder to bend the flagellum with the stiffer nexin links. Therefore, the bending amplitude of the wave-pattern decreases with the elastic sliding resistance, and the mean flagellar curvature also decreases compared to the cells with the normal flagellum. The variations ΔK_0 and ΔA_0 with respect to the elastic sliding resistance are displayed in Figures 5B-I and 5B-III. It is noted that the mean flagellar curvature K_0 increases during the interaction when k is larger than 100 N m^{-2}. In the case of the flagellum with the stiffer nexin links, the angular speed of the sperm head is decreased due to the reduced bending amplitude of the propagating wave. The two sperm heads will not exchange their positions as they do with the normal flagellum. Therefore, the interaction force preferable to one direction increases the time-asymmetry of the force $\mathbf{F}_{prx}$. Regardless of the elastic sliding resistance, the bending amplitude decreases after the formation of the collinear bundle because the interaction force suppresses the bending of the propagating wave. Figures 5B-II and 5B-IV show the variation of the average force $\Delta\langle\mathbf{F}_{prx}\rangle$ and the variation of the force amplitude $\Delta\mathrm{RMS}(\mathbf{F}_{prx})$ with respect to the different elastic sliding resistance k, which corresponds with the sign of ΔK_0 and ΔA_0, respectively. Our model can help us have a comprehensive understanding of the influence of different flagellar properties on the wave-patterns and explain the variation of wave-patterns of sperm cells in the collinear bundle.

3. Experimental Results

3.1. Free Sperm Cells

In the female reproductive tract, sperm cells need to go through the vagina, cervix, uterus, the utero-tubal junctions, and oviduct.[35] Due to the heterogeneity of biochemical composition, the viscosity of the fluid varies when sperm cells arrive at the different locations of the reproductive tract. As the viscosity of the fluid increases, the hydrodynamic drag will change, thus affecting the wave-patterns of sperm cells. Nevertheless, sperm cells are able to adapt to the fluidic environments with a range of viscosities in the reproductive tract. We experimentally observe the wave-patterns of free sperm cells and collinear bundles in SP-TALP solution with the viscosity of 1.2 mPa s and dextran solution with the viscosity of 25 mPa s (see Experimental Section). After determining the positions of the flagellum centerline, the Fourier analysis is implemented to extract wave

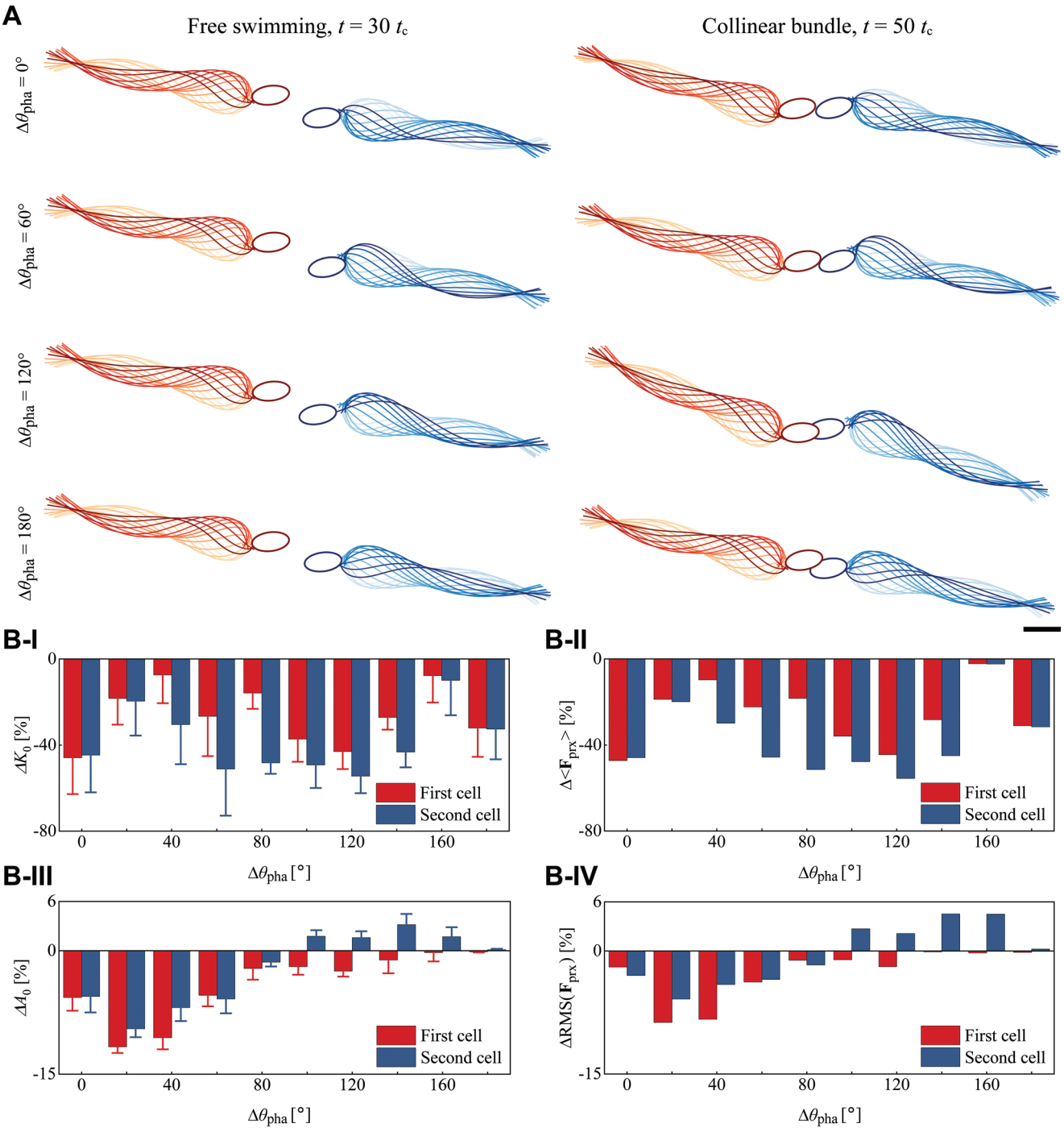

Figure 4. The numerical results in case of propagating waves of two cells with different phase shifts $\Delta\theta_{pha}$. A) The wave-patterns of two cells in case of the different phase shifts $\Delta\theta_{pha}$. The scale bar is 10 μm. B) The numerical results of the wave variables and force under $\Delta\theta_{pha}$ ranging from 0° to 180°. B-I) The variation percentage of the mean flagellar curvature, ΔK_0, for two cells. B-II) The variation percentage of the average forces, $\Delta\langle \mathbf{F}_{prx} \rangle$, acting on the proximal end of two cells. B-III) The variation percentage of the bending amplitude, ΔA_0, for two cells. B-IV) The variation percentage of the root mean square of the forces, $\Delta \mathrm{RMS}(\mathbf{F}_{prx})$, acting on the proximal end of two cells.

variables of sperm cells. The wave variables of sperm cells under zero force and a time-periodic interaction force are shown in the **Table 1**. In SP-TALP solution, the wave variables K_0, A_0, and λ of the free cells are 6.4 ± 3.5 rad mm^{-1}, 13.8 ± 2.8 rad mm^{-1}, and 73 ± 7 μm, respectively. In dextran solution, wave-patterns of free cells can be reconstructed by that with K_0 of 3.3 ± 3.0 rad mm^{-1}, A_0 of 9.4 ± 3.8 rad mm^{-1}, and λ of 57 ± 8 rad mm^{-1}. As the viscosity of medium increases, the wave variables K_0, A_0, and λ show the downward trend in accordance with the conclusion from others.[36,37]

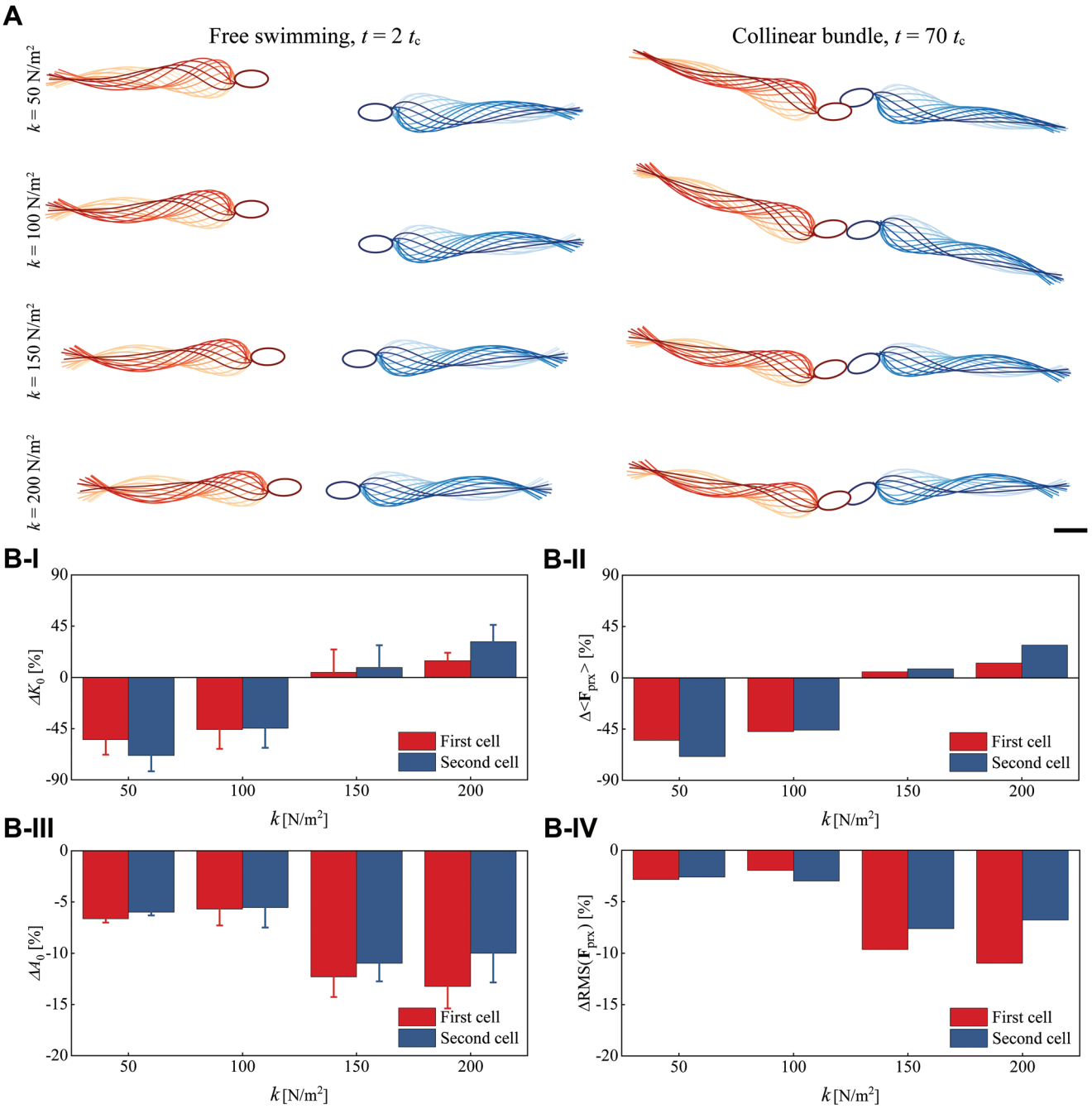

Figure 5. The numerical results in case of two sperm cells with the varying elastic sliding resistance k. A) The wave-patterns of two cells in case of different k. The scale bar is 10 µm. B) The numerical results under k from 50 to 200 N m^{-2}. B-I) The variation percentage of the mean flagellar curvature, ΔK_0, for two cells. B-II) The variation percentage of the average forces, $\Delta\langle \mathbf{F}_{prx} \rangle$, acting on the proximal end of two cells. B-III) The variation percentage of the bending amplitude, ΔA_0, for two cells. B-IV) The variation percentage of the root mean square of the forces, $\Delta\text{RMS}(\mathbf{F}_{prx})$, acting on the proximal end of two cells.

3.2. Sperm Cells under Time-Periodic Interaction

In the SP-TALP medium, the collinear bundle (see **Figure 6**A) exhibits the time-periodic wave-patterns. The wave variables of two cells at the continuous beat cycles are extracted in **Figure 7**A. Noted that no considerable difference in the wave-patterns of two cells is observed over the movement. The collinear bundle shows the steady swimming velocity of around 25.7 µm s^{-1}, as depicted in Figure 7B. The first cell (the upper cell in Figure 6A) presents the wave-pattern with the mean flagellar curvature, $K_0 = 1.8 \pm 1.1$ rad mm^{-1}, the bending amplitude, $A_0 = 9.6 \pm 1.4$ rad mm^{-1}, and the wavelength, $\lambda = 53 \pm 5$ µm. For the second cell (the bottom one in Figure 6A), the mean flagellar curvature, the bending amplitude, and the wavelength of the second cell are 1.2 ± 0.8 rad mm^{-1}, 5.0 ± 0.4 rad mm^{-1}, and 79 ± 4 µm, respectively. In the presence of the interaction

Table 1. Wave variables and swimming performance of the flagellar propulsion with the beat frequency of f under zero and the time-periodic interaction force. In the experiments, the wave variables and swimming performance of free sperm cells are averaged over three consecutive beat cycles ($n = 11$), while the average wave variables and swimming performance of sperm cells under interaction force are calculated from 20 beat cycles in each collinear bundle ($n = 3$). In the model, the wave variables and swimming performance of free sperm cells and sperm cells under interaction force are averaged at the first and the second phase, respectively. To compare the mean values obtained with sperm cells and collinear bundles, we used the two-sided Student's t-tests. The statistical t-test indicates the significant difference in the flagellar propulsion between free sperm cells and collinear bundles.

Viscosity	Configuration	Cell index	K_0 [rad mm^{-1}]	A_0 [rad mm^{-1}]	λ [μm]	f [Hz]	v [μm s^{-1}]
$\eta = 1.2$ mPa s	Free cell (Experiment)	–	6.39 ± 3.47	13.80 ± 2.81	72.99 ± 6.48	14.49 ± 4.18	115.99 ± 28.22
	Collinear bundle (Experiment)	1	1.75 ± 1.15	9.57 ± 1.38	53.39 ± 4.83	4.57 ± 0.55	25.62 ± 3.51
		2	1.20 ± 0.80	4.97 ± 0.45	79.15 ± 3.80	4.56 ± 0.34	
	Collinear bundle (Theory)	1	0.48 ± 0.15	7.12 ± 0.12	52.23 ± 0.04	4.57	3.34 ± 2.57
		2	1.00 ± 0.55	6.67 ± 0.14	55.14 ± 0.05	4.56	
$\eta = 25$ mPa s	Free cell (Experiment)	–	3.33 ± 3.07	9.37 ± 3.85	56.86 ± 8.28	13.09 ± 4.35	69.58 ± 33.20
	Collinear bundle (Experiment)	1	1.85 ± 0.78	5.32 ± 1.17	54.19 ± 5.06	2.63 ± 0.42	18.69 ± 8.80
		2	1.29 ± 0.88	3.76 ± 0.98	86.74 ± 21.78	2.61 ± 0.37	
	Collinear bundle (Theory)	1	0.64 ± 0.01	6.18 ± 0.01	49.13 ± 0.01	2.63	0.53 ± 0.13
		2	0.67 ± 0.01	5.43 ± 0.01	51.00 ± 0.02	2.61	

force, the symmetry of the wave-pattern of the collinear bundle is higher in comparison with the free sperm cell. Furthermore, the bending amplitude of the propagating wave decreases after forming the collinear bundle. It implies that the interaction force restricts the bending of the propagating wave to a great extent. The velocity of a sperm cell is directly related to its beat frequency, wavelength, and bending amplitude, where the relationship $v \sim A_0^2 f\lambda$ holds.[38] According to the extracted wave variables, the first cell possesses the faster swimming velocity than the second cell owing to its larger bending amplitude and smaller wavelength. Figure 7C illustrates the actual wave-patterns of the collinear bundle at three beat cycles. The collinear bundle in low viscosity fluid presents nearly unchanged wave-pattern within its entire swimming, which is in accordance with the small variation of the wave variables over 20 beat cycles. In addition, the propulsive thrust components ${}^{i}F_{\text{pro}}^{1}$ and ${}^{i}F_{\text{pro}}^{2}$, which compose the propulsive force, ${}^{i}\mathbf{F}_{\text{pro}} = {}^{i}F_{\text{pro}}^{1}\,{}^{i}\mathbf{e}_1 + {}^{i}F_{\text{pro}}^{2}\,{}^{i}\mathbf{e}_2$, are calculated over 20 beat cycles based on the resistive-force

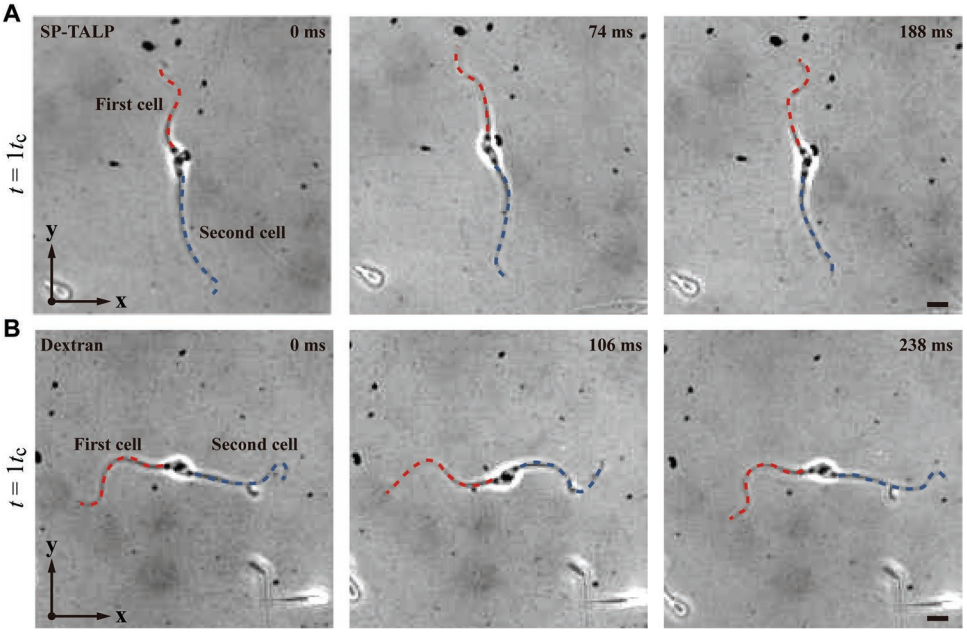

Figure 6. The respective propagating waves of the collinear bundle in A) SP-TALP solution with the viscosity of 1.2 mPa s and B) dextran solution with the viscosity of 25 mPa s in time sequences. The scale bar is 10 μm. See Video S1, Supporting Information.

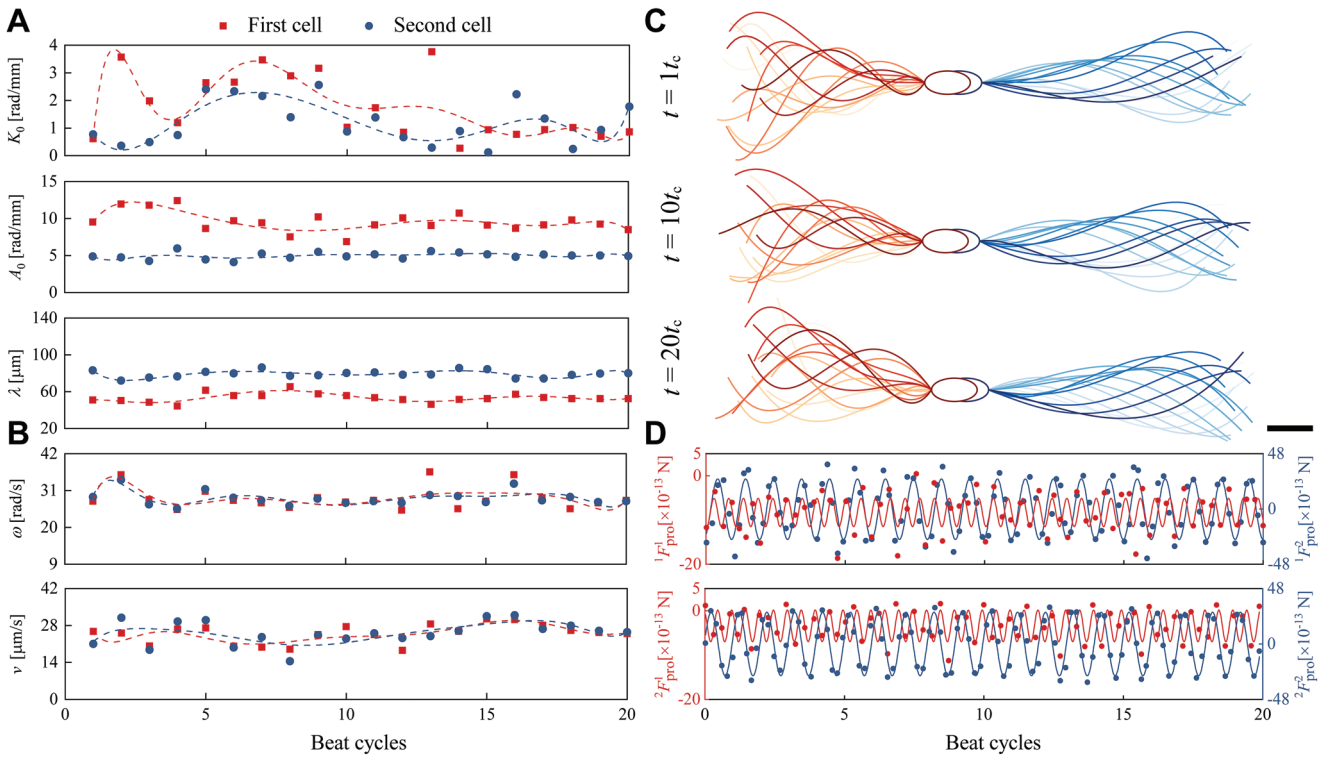

Figure 7. The measured results of the collinear bundle in SP-TALP solution (n = 3). A) Wave variables of the collinear bundle are measured over 20 beat cycles. B) Swimming characteristic of the collinear bundle. C) The actual wave-patterns of the collinear bundle at three beat cycles. The scale bar is 10 μm. D) The propulsive forces generated by the flagella of the collinear bundle are calculated over 20 beat cycles. The components ${}^iF^1_{pro}$ and ${}^iF^2_{pro}$ are along the orthonormal vectors ${}^i\mathbf{e}_1$ and ${}^i\mathbf{e}_2$ of the ith cell, respectively.

theory (see Figure 7D). The minor variation on the wave variables corresponds with the approximately time-periodic variation of the propulsive thrust. Among the force competition between $\langle {}^1F^1_{pro} \rangle = (8.3 \pm 1.4) \times 10^{-13}$ N and $\langle {}^2F^1_{pro} \rangle = (3.5 \pm 0.6) \times 10^{-13}$ N, the first cell with the greater average propulsive force pushes the second cell and determines the moving direction of the collinear bundle.

The other collinear bundle (see Figure 6B) is formed in the dextran solution. The two cells' variation curves of the wave variables versus beat cycles are plotted in **Figure** 8A. In the course of the movement, the first cell (the left cell in Figure 6B) displays the wave-pattern with the slight variation. In terms of the second cell (the right cell in Figure 6B), the wave variables but the wavelength show a negligible discrepancy over the swimming course. At the first time period (FTP, the first to the eighth beat cycle), the wavelengths of the first and the second cell are 54 ± 6 μm and 104 ± 12 μm, respectively. The collinear bundle swims with the velocity of 27.5 ± 4.1 μm s^{-1}, as shown in Figure 8B. At the second time period (STP, the 9th to the 11th beat cycle), the wave-pattern of the second cell goes through a transition from the large wavelength ${}^2\lambda = 104 \pm 12$ μm to the small wavelength ${}^2\lambda = 54 \pm 3$ μm. Although the two cells show similar wave-patterns during this time period, the collinear bundle can move with the velocity of 12.4 ± 4.7 μm s^{-1}. At the third time period (TTP, the 12th to the 20th beat cycle), the wavelength of the second cell increases to 82 ± 16 μm. The swimming velocity of the collinear bundle decreases to 10.8 ± 2.0 μm s^{-1}. The changes in wave variables at different beat cycles arise from the heterogeneity of the wave-patterns, as depicted in Figure 8C. Figure 8D shows the propulsive thrust components of sperm cells in the collinear bundle based on the extracted wave variables. The thrust displays the sinusoidal variation, but the frequency is changed as the angular frequency of sperm cells after the eighth beat cycle. During the FTP, the average propulsive forces ${}^iF^1_{pro}$ of the first cell and the second cell are calculated to be 7.4×10^{-12} and 3.6×10^{-12} N, respectively. During the STP, the propulsive thrust components $\langle {}^1F^1_{pro} \rangle$ and $\langle {}^2F^1_{pro} \rangle$ decrease to 2.8×10^{-12} and 2.3×10^{-12} N, respectively. During the TTP, the propulsive thrust component $\langle {}^1F^1_{pro} \rangle$ of the first cell is 3.9×10^{-12} N, while $\langle {}^2F^1_{pro} \rangle$ of the second cell is 3.1×10^{-12} N. From the standpoint of force, the decrease of resultant propulsive thrust on the collinear bundle explained the reduced velocity at the TTP in comparison with that at the FTP. However, the velocity of the collinear bundle at the TTP is smaller than that at the STP, while the resultant propulsive thrust is greater at the TTP. It can be attributed to the fact the velocity of the collinear bundle is mainly determined by the angular frequency of the flagellar beat.

3.3. Flow Field and Bending Moment

The regularized Stokeslets theory (see Experimental Section) can predict the fluid response for a given point force along the flagellum. Therefore, we utilize the regularized Stokeslets theory to predict the fluid response for the point forces on the

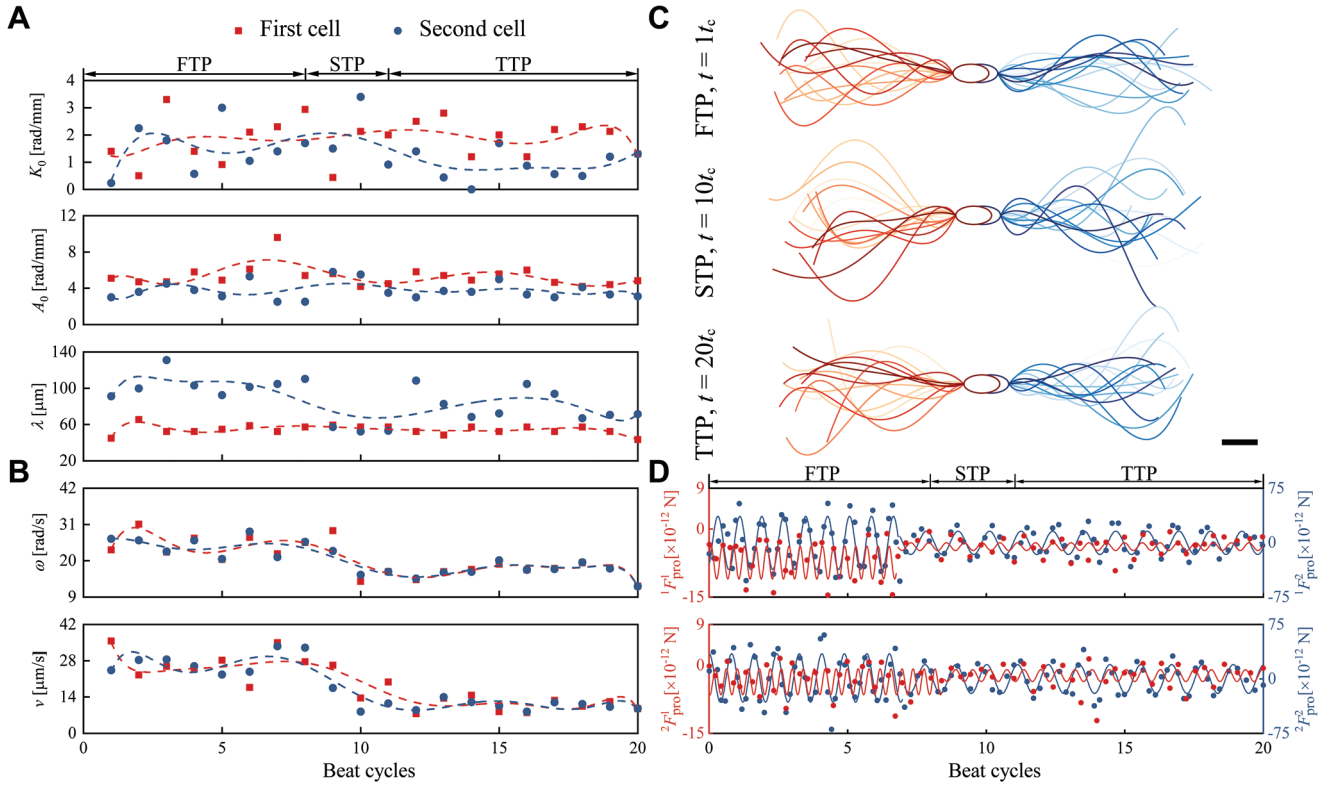

Figure 8. The collinear bundle in dextran solution (n = 3). A) Wave variables and B) swimming characteristic of two cells are measured at the first time period (FTP, the first to the eighth beat cycle), the second time period (STP, the 9th to the 11th beat cycle), and the third time period (TTP, the 12th to the 20th beat cycle). C) The actual wave-patterns of the collinear bundle in one beat cycle of three time periods. The scale bar is 10 μm. D) The propulsive forces components $^iF^1_{pro}$ and $^iF^2_{pro}$ generated by the flagella of the collinear bundle are calculated over 20 beat cycles.

sperm flagellum. The time-averaged flow fields $\mathbf{u}(x)$ around the free sperm cells and the collinear bundles are calculated as shown in **Figure 9**A–D. For the free sperm cell, the time-averaged flow field increases toward the distal end. This is because the rate of wave propagation increases as the bending stiffness decreases over the length.[39] Moreover, the increase in the flow field along the flagellum indicates that the bending wave is initiated at the proximal end. With the increase of the fluid viscosity, the time-averaged flow field decreases owing to the decrease of the bending amplitude of the propagating waves. Compared to the free sperm cells, the collinear bundle generates the smaller averaged flow field due to its smaller bending amplitude. For every single cell in the collinear bundle, the identical fluid behavior as a free sperm cell that the flow field increases

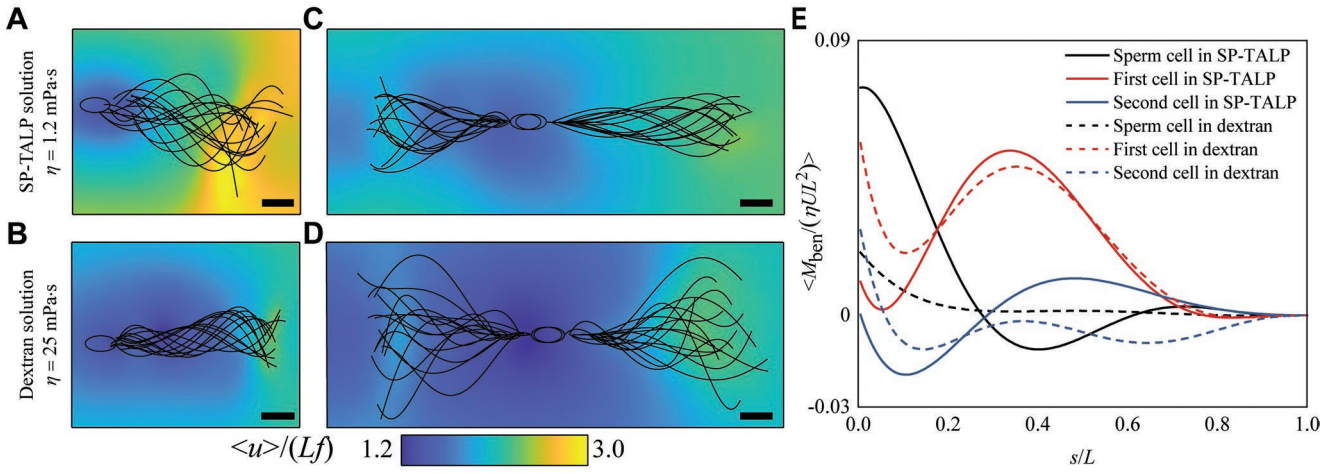

Figure 9. The time-averaged flow field of the free sperm cell in A) SP-TALP solution (n = 11) and B) dextran solution (n = 11) and the collinear bundle in C) SP-TALP solution (n = 3) and D) dextran solution (n = 3). The scale bar is 10 μm. E) Nondimensional time-averaged bending moments $\langle M_{ben}/(\eta UL^2)\rangle$ are calculated over one beat cycle for the free sperm cell and the collinear bundle in SP-TALP and dextran solution.

from the proximal end to the distal end is noted in Figure 9C,D. Due to the zero-torque and zero-force condition at the distal end, the time-averaged flow field reaches the maximum at this location. It implies that the wave propagation is initiated and coordinated from the proximal end for the collinear bundle.

Additionally, the bending moment M_{ben} used for adjusting the wave-pattern can be derived from the positions of the flagellar centerline (see Experimental section). Figure 9E shows the respective nondimensional time-averaged bending moments $\langle M_{\text{ben}}/(\eta UL^2)\rangle$,[40] where U is the magnitude of the flagellum velocity, $\mathbf{U} = \mathbf{U}_{\perp} + \mathbf{U}_{\parallel}$ (see Experimental Section). In the case of the free sperm cell in the SP-TALP solution, the time-averaged bending moment decreases to zero at one-third of the flagellum. The maximum displacement of the flagellum can be observed at the corresponding position in Figure 9A. For the free sperm cell in the dextran solution, the time-averaged bending moment is always positive, accounting for the increase of the bending amplitude of the propagating wave toward the distal end. Figure 9E also describes the distributed nondimensional time-averaged bending moment along two flagella of the collinear bundle. The first cell (the left cell in Figure 9C,D) possesses the greater nondimensional time-averaged bending moment than the second cell (the right cell in Figure 9C,D). In the low-viscous fluid, the first cell motivates the positive bending moment along the entire flagellum. It is consistent with the first cell showing the increasing bending amplitude toward the distal end, as shown in Figure 9C. The wave-pattern of the second cell over one beat cycle exhibits the maximum bending amplitude at the $s/L = 0.3$ and the $s/L = 1$, which corresponds with the maximum displacement at the respective locations. In the high-viscous fluid, two cells generates the bending moment with the unchanged direction to produce the propagating wave with the increasing displacement over the flagellum. Compared to free sperm cells, sperm cells in the collinear bundle can overcome the interaction force by generating the greater time-averaged bending moment.

4. Discussion

Prior to fusing with the ovum, sperm cells are likely to experience various physical and chemical interactions in the female reproductive tracts. Spermatozoa interact with the oviductal epithelial cells, which can be understood as one selection mechanism. Only uncapacitated sperm cells can bind to the oviduct and be stored there. Upon ovulation and capacitation, sperm cells become hyperactivated and thereby detach from the oviductal epithelial cells. This process controls the timing of the arrival of matured sperm cells at the ovum.[41] On the other hand, sperm cells need to interact with the zona pellucida for successful fusion. Acrosomal enzymes are released during the acrosome reaction that allows the penetration of the zona pellucida in combination with hyperactivity, which allows mechanical penetration and removal of the cumulus cells.[42] These interactions will inevitably affect flagellar propulsion of sperm cells, and filter out the abnormal sperm cells with poor motility. High-quality sperm cells are able to migrate further in the female reproductive tract, and only one sperm cell can finally fertilize the ovum. Regardless of the interaction with fluid flow, the surface, or the cells, the effect acts on sperm cells in the form of a force. Herein, cell-to-cell interaction serves as a case to study the effect of a interaction force on flagellar propulsion of sperm cells. Through our developed model, we first study the configuration of sperm bundle when two cells interact. Two configurations, a collinear bundle and an aligned bundle, can be formed after the interaction. Irrespective of the initial orientations of two cells, the configuration of sperm bundle depends on the resultant interaction torque on sperm cells (Figure 2A). The collinear bundle can be formed when the interaction is dominant by steric interaction. In this case, one cell rotates clockwise, while the other cell rotates counterclockwise since its resultant torque is opposite (Figure 2B). On the contrary, if the adhesive interaction is stronger than the steric interaction, one cell rotates counterclockwise and the other cell rotates clockwise, thereby forming an aligned bundle.

To understand the effect of a time-periodic force on the flagellar propulsion of sperm cells, we measured the wave-patterns of the collinear bundles. By means of the Fourier analysis on the measured wave-patterns, we find that wave-patterns with smaller mean flagellar curvature and bending amplitude are exhibited by the sperm cells in the collinear bundles than free sperm cells. Likewise, our numerical results show the similar decrease in the mean flagellar curvature, bending amplitude, and swimming velocity for the collinear bundle, which qualitatively agrees with the experimental results (Table 1). After forming the collinear bundle, the interaction force, consisting of steric and adhesive force, is applied to the proximal end of the sperm flagellum and against the drag force exerted by the sperm head. The wave-pattern displays the shape with the high time-symmetry under the effect of the interaction force. Since the interaction force is opposite to the drag force, the bending amplitude of the propagating wave is suppressed, thereby leading to the wave-patterns with the smaller bending amplitude compared to free sperm cells. During the fusion with an ovum, the sperm head will be subjected to a time-periodic reaction force. Thus, it is likely that sperm cells exhibit the same wave-patterns in the female reproductive tract. Our theoretical model and experiments provide tools to investigate the behavior of the cell during interactions with its surroundings. These sperm cells with excellent motility can travel through the physical barrier in the reproductive tract and arrive at the fertilization site. Our work can inspire future research in the field and can be used for analyzing sperm motility by means of the wave-patterns analysis, reducing the complexity of the current semen analysis in the field of reproductive health.

Moreover, our theoretical study shows that the mean flagellar curvature and the bending amplitude are not invariably reduced in terms of the wave-pattern of sperm cells in the collinear bundles. When the initial phase of propagating wave of cells exceeds 90°, the mean flagellar curvature of wave-patterns of sperm cells decreases (Figure 4B-I), yet the bending amplitude increases after forming the collinear bundle (Figure 4B-III). In this case, the drag force reverses to be in the same direction as the interaction force. The force at the proximal end, comprising the drag force and the interaction force, increases after forming the collinear bundle (Figure 4B-IV), thereby facilitating the bending of the propagating wave. In addition, the mean flagellar curvature increases (Figure 5B-I), and the bending amplitude decreases

(Figure 5B-III) for the collinear bundle when the elastic sliding resistance exceeds 50 N m^{-2}. As the elastic sliding resistance of the flagellum increases, the nexin links can be considered as the stiffer spring. The sperm flagellum with the higher elastic sliding resistance will be harder to bend. Therefore, sperm cells display the wave-patterns with the smaller mean flagellar curvature and bending amplitude, and the angular speed of the sperm head is reduced. Two sperm heads will not experience the switch of the position during the overlap, which results in the interaction force pointing to one side. Under this manner, the time-asymmetrical interaction force is generated and applied to the proximal end of the sperm flagellum, enhancing the asymmetry of the wave-patterns. Our developed model can predict the variation of the wave-patterns of sperm cells with different flagellar properties after forming the collinear bundle, although we cannot control these variables of sperm cells in biological world.

In addition, our experimental results indicate that sperm cells can overcome the time-periodic interaction force by generating a greater internal bending moment. The importance of the distributed contractile elements in the flagellum is underlined when sperm cells face the external force. During the journey to the ovum, sperm cells are likely to contact the boundary, fluid flow, and other cells. Our results reveal the underlying mechanism of the adaptive behavior, when encountering a time-periodic force. In terms of the design of soft micro-nanorobots,[43–45] the component which can generate adjustable bending moments should be included to overcome the external force, so that soft microrobots with high adaptability can be better applied to in vivo biomedical applications when facing an external force.

Our hydrodynamic model captures the true behavior of two sperm cells when they form a collinear bundle in vitro. The numerical results reveal a decrease in the mean flagellar curvature and the bending amplitude of the cells, agreeing with the experimental results in low- and high-viscosity fluids. However, there is a deviation in the average path velocity of the collinear bundle between the experimental and numerical results (Table 1). The difference between experimental and numerical results is attributed to the deviation between the internal bending moment of the motile sperm cells which affect their motility. Moreover, the environments are more complicated in the female reproductive tract. In addition to the viscoelastic property of the biological fluid,[35] secretory cells and ciliated cells extensively distributed in the reproduction tract[46] also affect the wave-pattern of sperm cells on the path to the ovum. Although our model addresses a specific type of interaction, that is the collinear bundle, the presented theoretical and experimental framework can be used to obtain a different generalization for other types of interactions. For other configurations of sperm bundles or the interaction with secretory cells and ciliated cells, only the interaction force needs to be determined in the hydrodynamic model. As part of future studies, our model will be upgraded to systematically analyze wave-pattern of sperm cells when encountering various interactions in vivo.

5. Conclusions

Our hydrodynamic model and experiments allow us to understand the variation of the wave-patterns of sperm cells when swimming against a time-periodic interaction force. Our hydrodynamic model indicates that wave-pattern of sperm cells in the collinear bundle becomes symmetric, and the bending amplitude of the propagating wave decreases. Moreover, it manifests that the variation of wave-pattern is also influenced by other parameters such as the initial phase and the elastic sliding resistance. When the initial phase of the propagating wave exceeds 90°, the bending amplitude increases after forming the collinear bundle. For the flagellum with high elastic sliding resistance, the mean flagellar curvature increases in terms of the wave-patterns of collinear bundle. As the viscosity increases, the mean flagellar curvature, the bending amplitude, and the velocity of the collinear bundle are reduced according to the numerical results. Similarly, we experimentally find that the mean flagellar curvature and bending amplitude of wave-patterns of sperm cells decrease after forming a collinear bundle. Furthermore, wave variables of the collinear bundle decrease with the viscosity of the fluid, and the swimming performance of collinear bundle diminishes due to reduced frequency of the flagellar beat. Our study provides crucial insights into the hydrodynamic interactions of sperm cells not only with time-periodic interaction forces, but also with other dynamic interaction forces encountered in vivo. Further understanding of such cell-to-cell interaction will elucidate crucial processes preceding fertilization. Although we investigate a specific mode of cell-to-cell interaction, sperm cells physically interact with other bodies in the surrounding fluid. They bind to the cilia of the oviduct and interact with the cumulus cells and zona pellucida. Even though these interactions are complex in nature, physically, they can also be seen as dynamic and impose forces onto the sperm cells. Our study contributes to understanding the spermatozoa's response to such external physical forces and the resulting change in their flagellar motion. This knowledge can also advance the understanding of a sperm cell's ability to overcome these forces. Furthermore, our work provides a novel way to study the sperm motility when encountering external dynamic forces, and inspires technological improvements in assisted reproduction.

6. Experimsental Section

Sperm Cell Video Microscopy: Cryopreserved bovine sperm cells were thawed in a 37 °C water bath for 2 min before resuspending the thawed semen in 1 mL SP-TALP (modified sperm Tyrode's albumin lactate phosphate medium, Caisson Labs). The sample was centrifuged at 300 *g* for 5 min; the supernatant was removed and resuspended in 1 mL fresh SP-TALP which resulted in a sperm concentration of about 3×10^6 sperms per mL. Sperm cells were then diluted 1:1 in either 10 µL SP-TALP (resulting in 1.2 mPa s viscosity) or 10 µL 20% dextran solution (dextran from *Leuconostoc* spp., Mr 70000. 31390-25G from Sigma-Aldrich resulting in 10% dextran with about 25 mPa s viscosity at 40 °C.[47]). The samples were mixed and filled into a 10 µL Leja slide. Video microscopy was performed in a Zeiss microscope with a phase contrast 40× objective and high-speed camera to obtain videos with 500 images per second.

Fourier Analysis of Wave-Pattern: Sperm flagella were characterized by the tangent angles, ${}^i\varphi(s, t)$, enclosed between the local tangent of the flagellum of *i*th cell and the orthonormal vector ${}^i\mathbf{e}_1$. The tangent angle can be approximately described using its zeroth and the first Fourier mode as follows:[36,48]

$$\begin{aligned} {}^i\varphi(s,t) &\approx {}^i\varphi_0(s) + {}^i\varphi_1(s)e^{i\omega t} + {}^i\varphi_1^*(s)e^{-i\omega t} \\ &\approx K_0 s + 2A_0 s\cos(\omega t - 2\pi s/\lambda) \end{aligned} \tag{15}$$

Three key parameters that determine the wave-patterns of a sperm cells can be extracted from the Fourier decomposition. The zeroth Fourier mode, ${}^i\varphi_0(s) = K_0 s$, characterizes the time-averaged mean shape of the flagellum. The mean flagellar curvature K_0 denotes the symmetry of wave-patterns over one beat cycle. Second, the bending amplitude A_0 along the tail is extracted from the absolute value of the first mode, $|{}^i\varphi_1(s)| = A_0 s$, reflecting the bending of the flagellum. Third, λ is the wavelength and obtained by fitting $2\pi s/\lambda$ to the phase angle of the complex first Fourier mode $-\arg {}^i\varphi_1^*(s)$.

Calculation of the Drag-Based Thrust: The resistive-force theory is also known as local drag theory. Suppose that the flagellum is subject to an external drag which is uniformly distributed over the flagellum. The external drag can be decomposed into two components tangent and normal to the surface of the flagellum. The tangent vectors are expressed by ${}^i\mathbf{t}(s,t) = (\partial {}^i\mathbf{r}(s,t)/\partial s)/\left|\partial {}^i\mathbf{r}(s,t)/\partial s\right|$, and the normal vectors ${}^i\mathbf{n}(s,t)$ along the ith flagellum are determined through the expression ${}^i\mathbf{n}(s,t) = (\partial {}^i\mathbf{t}(s,t)/\partial s)/\left|\partial {}^i\mathbf{t}(s,t)/\partial s\right|$. The velocities along the local tangent and normal velocity of ith flagellum are calculated by

$$ {}^i\mathbf{U}_{\parallel}(s,t) = \left({}^i\dot{\mathbf{r}}(s,t)\cdot {}^i\mathbf{t}(s,t)\right){}^i\mathbf{t}(s,t),\ {}^i\mathbf{U}_{\perp}(s,t) = {}^i\dot{\mathbf{r}}(s,t) - {}^i\mathbf{U}_{\parallel}(s,t) \tag{16} $$

Then, the propulsive thrust generated by one segment of the ith flagellum is as follows:

$$ {}^i\mathbf{f}(s,t) = {}^i\xi_{\perp}\ {}^i\mathbf{U}_{\perp}(s,t) + {}^i\xi_{\parallel}\ {}^i\mathbf{U}_{\parallel}(s,t) \tag{17} $$

The tangent and normal drag coefficients of ith flagellum are given by[49]

$$ {}^i\xi_{\perp} = \frac{4\pi\eta}{\ln\left(\frac{2L}{d}\right) + 0.193},\quad {}^i\xi_{\parallel} = \frac{2\pi\eta}{\ln\left(\frac{2L}{d}\right) - 0.807} \tag{18} $$

where d is the diameter of the flagellum.

Calculation of the Fluid Response: Regularized Stokeslets theory was implemented to predict the produced flow field. Assuming the surface of collinear bundle are covered with N Stokeslets boundary points, the flow field $\mathbf{u}(\mathbf{x})$ caused by traction forces $\mathbf{F}_k$ at the position $\mathbf{r}_k$ is given by[50]

$$ \begin{aligned} \mathbf{u}(\mathbf{x}) = &\sum_{k=1}^{N}\frac{-\mathbf{F}_k}{2\pi\eta}\left[\ln\left(\sqrt{r_k^2+\varepsilon^2}+\varepsilon\right) - \frac{\varepsilon\left(\sqrt{r_k^2+\varepsilon^2}+2\varepsilon\right)}{\left(\sqrt{r_k^2+\varepsilon^2}+\varepsilon\right)^2}\right] \\ &+ \frac{1}{4\pi\eta}\left[\mathbf{F}_k\cdot(\mathbf{x}-\mathbf{r}_k)\right](\mathbf{x}-\mathbf{r}_k)\left[\frac{\sqrt{r_k^2+\varepsilon^2}+2\varepsilon}{\left(\sqrt{r_k^2+\varepsilon^2}+\varepsilon\right)^2\sqrt{r_k^2+\varepsilon^2}}\right] \\ &= \mathbf{G}(\mathbf{x})\mathbf{F}_k \end{aligned} \tag{19} $$

where $r_k = |\mathbf{x} - \mathbf{r}_k|$ is the distance between the observation point $\mathbf{x}$ and source points $\mathbf{r}_k$, ε represents the surface area where the force is distributed, $\varepsilon = 0.25ds \simeq 0.25\Delta s$, and $\Delta s = 2r$. $\mathbf{G}(\mathbf{x})$ is the regularized Green's function.

Bending Moment of the Flagellum: The coordinates of the flagellar centerline were acquired from the videos of sperm cells. For each frame in the videos, 20 equal points with the coordinates of (x, y) along the flagellum were marked and tracked via custom-written MATLAB routine (The MathWorks, Inc., Natick, MA, USA). The bending moment M_{ben} along the flagellum could be determined through the following expression:[51]

$$ \frac{\partial^2 M_{\text{ben}}(x,t)}{\partial x^2} = \xi_{\perp}\frac{\partial y(x,t)}{\partial t} + E\frac{\partial^4 y(x,t)}{\partial x^4} \tag{20} $$

The bending moment can be utilized to study the internal activity of the sperm flagellum.

Statistical Analysis: The time-averaged velocity $\langle v\rangle$, and the distributed bending moment, M_{ben}, of all groups were processed in the normalization method. Unless otherwise indicated, all the presented data are displayed as mean ± s.d. The sample sizes (n) are provided in the figure legends. To assess the differences in the flagellar propulsion between free sperm cells and collinear bundles, the two-sided Student's t-test was conducted. The difference was regarded to be statistically significant if $p < 0.05$. Custom-made MATLAB routine was used to perform statistical analysis.

Supporting Information

Supporting Information is available from the Wiley Online Library or from the author.

Acknowledgements

Z.W. thanks the financial support of the China Scholarship Council under Grant No. 202006120058. V.M. thanks the "la Caixa" Foundation (ID 100010434) and the European Union's Horizon 2020 research and innovation programme under the Marie Skłodowska-Curie grant agreement No LCF/BQ/PI21/11830003. This work was also supported by the European Research Council (ERC) under the European Union's Horizon 2020 Research and Innovation programme under Grant 866494 project-MAESTRO.

Conflict of Interest

The authors declare no conflict of interest.

Data Availability Statement

The data that support the findings of this study are available from the corresponding author upon reasonable request.

Keywords

bovine sperm cells, cell-to-cell interaction, flagellar propulsion, hydrodynamic models

Received: August 19, 2022
Revised: September 3, 2022
Published online: October 20, 2022

[1] O. Felfoul, M. Mohammadi, S. Taherkhani, D. De Lanauze, Y. Zhong Xu, D. Loghin, S. Essa, S. Jancik, D. Houle, M. Lafleur, et al., *Nat. Nanotechnol.* **2016**, *11*, 941.
[2] E. H. Harris, *Annu. Rev. Plant Biol.* **2001**, *52*, 363.
[3] E. A. Gaffney, H. Gadêlha, D. Smith, J. Blake, J. C. Kirkman-Brown, *Annu. Rev. Fluid Mech.* **2011**, *43*, 501.
[4] R. Kamiya, S. Asakura, *J. Mol. Biol.* **1976**, *106*, 167.
[5] R. Kamiya, S. Asakura, *J. Mol. Biol.* **1976**, *108*, 513.
[6] H. Hotani, *Biosystems* **1980**, *12*, 325.
[7] K. Shimada, R. Kamiya, S. Asakura, *Nature* **1975**, *254*, 332.
[8] V. Kantsler, J. Dunkel, M. Blayney, R. E. Goldstein, *Elife* **2014**, *3*, e02403.
[9] E. Hasegawa, R. Kamiya, S. Asakura, *J. Mol. Biol.* **1982**, *160*, 609.
[10] N. C. Darnton, H. C. Berg, *Biophys. J.* **2007**, *92*, 2230.
[11] H. Hotani, *J. Mol. Biol.* **1982**, *156*, 791.

[12] R. M. Macnab, M. K. Ornston, *J. Mol. Biol.* **1977**, *112*, 1.
[13] S. H. Larsen, R. W. Reader, E. N. Kort, W.-W. Tso, J. Adler, *Nature* **1974**, *249*, 74.
[14] L. Turner, W. S. Ryu, H. C. Berg, *J. Bacteriol.* **2000**, *182*, 2793.
[15] G. Langousis, K. L. Hill, *Nat. Rev. Microbiol.* **2014**, *12*, 505.
[16] M. E. Teves, F. Barbano, H. A. Guidobaldi, R. Sanchez, W. Miska, L. C. Giojalas, *Fertil. Steril.* **2006**, *86*, 745.
[17] K. Miki, D. E. Clapham, *Curr. Biol.* **2013**, *23*, 443.
[18] S. Boryshpolets, S. Pérez-Cerezales, M. Eisenbach, *Hum. Reprod.* **2015**, *30*, 884.
[19] A. Bahat, I. Tur-Kaspa, A. Gakamsky, L. C. Giojalas, H. Breitbart, M. Eisenbach, *Nat. Med.* **2003**, *9*, 149.
[20] J. Elgeti, U. B. Kaupp, G. Gompper, *Biophys. J.* **2010**, *99*, 1018.
[21] V. F. Geyer, F. Jülicher, J. Howard, B. M. Friedrich, *Proc. Natl. Acad. Sci. USA* **2013**, *110*, 18058.
[22] A. Hilfinger, A. K. Chattopadhyay, F. Jülicher, *Phys. Rev. E* **2009**, *79*, 051918.
[23] B. J. Walker, K. Ishimoto, E. A. Gaffney, *Phys. Rev. Fluids* **2020**, *5*, 123103.
[24] W. H. Organization, Infertility, https://www.who.int/health-topics/infertility (accessed: July 2022).
[25] D. J. Pearce, L. Hoogerbrugge, K. A. Hook, H. S. Fisher, L. Giomi, *J. R. Soc. Interface* **2018**, *15*, 20180702.
[26] D. Miller, H. Burkin, *Reprod. Suppl.* **2001**, *58*, 147.
[27] B. Nixon, H. Ecroyd, J.-L. Dacheux, F. Dacheux, V. Labas, S. D. Johnston, R. C. Jones, *Biol. Reprod.* **2016**, *95*, 91.
[28] D. M. Higginson, S. Pitnick, *Biol. Rev.* **2011**, *86*, 249.
[29] C. J. Brokaw, *J. Exp. Biol.* **1971**, *55*, 289.
[30] H. Gadêlha, E. A. Gaffney, A. Goriely, *Proc. Natl. Acad. Sci. USA* **2013**, *110*, 12180.
[31] J. Gray, G. Hancock, *J. Exp. Biol.* **1955**, *32*, 802.
[32] J. Elgeti, G. Gompper, *Eur. Phys. J. Spec. Top.* **2016**, *225*, 2333.
[33] S. Camalet, F. Jülicher, *New J. Phys.* **2000**, *2*, 24.
[34] K. Inaba, *Mol. Hum. Reprod.* **2011**, *17*, 524.
[35] S. S. Suarez, A. Pacey, *Hum. Reprod. Update* **2006**, *12*, 23.
[36] B. M. Friedrich, I. H. Riedel-Kruse, J. Howard, F. Jülicher, *J. Exp. Biol.* **2010**, *213*, 1226.
[37] F. Striggow, M. Medina-Sánchez, G. K. Auernhammer, V. Magdanz, B. M. Friedrich, O. G. Schmidt, *Small* **2020**, *16*, 2000213.
[38] R. Rikmenspoel, *Biophys. J.* **1965**, *5*, 365.
[39] J. M. S. Dias, D. Estima, H. Punte, A. Klingner, L. Marques, V. Magdanz, I. S. M. Khalil, *Adv. Theor. Simul.* **2022**, *5*, 2100438.
[40] C. Brokaw, *J. Exp. Biol.* **1970**, *53*, 445.
[41] R. Lefebvre, S. S. Suarez, *Biol. Reprod.* **1996**, *54*, 575.
[42] S. Suarez, H.-C. Ho, *Reprod. Domest. Anim.* **2003**, *38*, 119.
[43] J. Zhang, Z. Ren, W. Hu, R. H. Soon, I. C. Yasa, Z. Liu, M. Sitti, *Sci. Rob.* **2021**, *6*, eabf0112.
[44] J. Zhang, Y. Guo, W. Hu, M. Sitti, *Adv. Mater.* **2021**, *33*, 2100336.
[45] S. Martel, *Biomicrofluidics* **2016**, *10*, 021301.
[46] H. Hagiwara, N. Ohwada, T. Aoki, T. Suzuki, K. Takata, *Med. Mol. Morphol.* **2008**, *41*, 193.
[47] A. Farahnaky, Z. Allahdad, M. Aminlari, M. Majzoobi, H. Askari, R. Ramezani, *Int. J. Food Eng.* **2012**, *8*, 3.
[48] I. S. M. Khalil, V. Magdanz, J. Simmchen, A. Klingner, S. Misra, *Appl. Phys. Lett.* **2020**, *116*, 063702.
[49] C. Brennen, H. Winet, *Annu. Rev. Fluid Mech.* **1977**, *9*, 339.
[50] R. Cortez, *SIAM J. Sci. Comput.* **2001**, *23*, 1204.
[51] V. Magdanz, J. Vivaldi, S. Mohanty, A. Klingner, M. Vendittelli, J. Simmchen, S. Misra, I. S. M. Khalil, *Adv. Sci.* **2021**, *8*, 2004037.